Journal of Geophysical Research: Atmospheres

RESEARCH ARTICLE
10.1029/2018JD028324

Key Points:
- Precipitating versus nonprecipitating, stratiform versus convective, and shallow versus deep convection in TCs are classified using NRL 37 GHz color product
- Generally pure pink is deep convection, bright cyan is shallow convection, while hybrid pink is stratiform precipitation
- A significant increase of stratiform precipitation and shallow convection is found prior to the onset of TC rapid intensification

Correspondence to:
H. Jiang,
haiyan.jiang@fiu.edu

Citation:
Jiang, H., Zagrodnik, J. P., Tao, C., & Zipser, E. J. (2018). Classifying precipitation types in tropical cyclones using the NRL 37 GHz color product. *Journal of Geophysical Research: Atmospheres*, *123*, 5509–5524. https://doi.org/10.1029/2018JD028324

Received 19 JAN 2018
Accepted 27 APR 2018
Accepted article online 6 MAY 2018
Published online 25 MAY 2018

Classifying Precipitation Types in Tropical Cyclones Using the NRL 37 GHz Color Product

Haiyan Jiang[1], Joseph P. Zagrodnik[1,2], Cheng Tao[1,3], and Edward J. Zipser[4]

[1]Department of Earth and Environment, Florida International University, Miami, FL, USA, [2]Department of Atmospheric Sciences, University of Washington, Seattle, WA, USA, [3]Lawrence Livermore National Laboratory, Livermore, CA, USA, [4]Department of Atmospheric Sciences, University of Utah, Salt Lake City, UT, USA

Abstract The tropical cyclone (TC) webpage developed by the U.S. Naval Research Lab (NRL) has been widely used by the community for real-time TC monitoring and forecasting. Using 14 years of Tropical Rainfall Measuring Mission Microwave Imager and Precipitation Radar data in TCs, precipitation/convection types are quantitatively classified based on vertical radar profiles corresponding to seven different color regions in the NRL's 37 GHz color composite product. The bright cyan and all pink (including pure pink, bright cyan/pink, and weak cyan/pink, and green/pink) regions are identified as nearly 100% precipitative regions. The bright cyan and pure pink regions are shallow and deep convective precipitation, respectively, while the green/pink, weak cyan/pink, and bright cyan/pink regions are mainly stratiform rain. Eighty-four percent of pixels in the weak cyan region are precipitating, including either shallow convective, stratiform, or anvil precipitation. Seventy-six percent of pixels in the green region are nonprecipitating pixels, and 24% of them are very lightly precipitating pixels, which could be contaminated from clouds with high liquid water content. The ability to perform TC precipitation-type analysis of this detail (convective versus stratiform and deep versus shallow) was previously only possible using radar-based classification algorithms. Using the 37 GHz precipitation-type analysis, a significant increase of coverage of stratiform precipitation and shallow convection in the inner core is found between 3 and 21 hr before the onset of TC rapid intensification.

1. Introduction

Satellite observations have provided an excellent data source for monitoring and predicting tropical cyclones (TCs). Based on infrared (IR) and visible satellite imagery, the Dvorak TC intensity estimation technique has been the primary method of monitoring tropical systems globally since 1970s (Dvorak, 1975). The high temporal resolution and large spatial coverage of geostationary IR and visible images make them optimal for operational TC monitoring. However, IR and visible sensors can only detect the cloud top temperature/height and cloud reflectance, respectively. In contrast, passive microwave channels allow penetration into nonprecipitating or precipitating clouds, therefore providing information about ice and liquid hydrometeors instead of just the cloud tops.

The passive microwave channels available on satellites for precipitation observations mainly include frequencies around 10, 19, 37, 85, and 91 GHz. Passive microwave sensors carrying these channels include the Tropical Rainfall Measuring Mission (TRMM) Microwave Imager (TMI), Global Precipitation Measurement Microwave Imager (GMI), Advanced Microwave Scanning Radiometer 2 (AMSR2), Special Sensor Microwave Imager (SSM/I), and Special Sensor Microwave Imager/Sounder (SSMIS). At 10–19 GHz, scattering by cloud and precipitation-sized particles is usually small relative to emission by rain, especially at the resolution of these sensors. Although brightness temperatures (T_B) of these channels in the whole TC region were found better correlated with TC intensity than T_B of higher frequency channels, due to the large footprint size, 10 and 19 GHz channels are not very useful for addressing the structural details of a TC (Hoshino & Nakazawa, 2007). At 85–91 GHz, the liquid water emission effect is small relative to ice scattering. The ice-scattering signature at this channel has been used as a proxy of convective intensity for both TCs (Cecil et al., 2002; Cecil & Zipser, 2002; Jiang, 2012; Jiang et al., 2013) and other precipitation systems (Zipser et al., 2006). Unlike lower or higher frequency channels having the scene dominated by one effect or the other, the 37 GHz channel is unique because it has more of a mix of the ice scattering and liquid water/rain emission effects in a typical hurricane scene. Its T_B increases due to emission and decreases due to ice scattering (Weng & Grody, 1994).

Table 1
Description of Features in the 37color Imagery and Their Brightness Temperature Ranges as Observed in TCs

Product/features	Sea surface	Liquid clouds or warm rain	Deep clouds with ice above and liquid hydrometeors below the freezing level
37color	Dark green	Cyan	Pink
PCT37	270–300 K	275–290 K	165–275 K
V37	<245 K	245–285 K	165–275 K
H37	<225 K	225–285 K	160–275 K

However, most previous TC studies only made use of the 37 GHz's ice-scattering signature (Cecil et al., 2002; Cecil & Zipser, 2002; Jiang, 2012; Jiang et al., 2013). The polarization-corrected brightness temperature (PCT; Spencer et al., 1989) at this channel is generally used as an indicator of total ice amount above the freezing level. The 37 GHz color composite (hereafter 37color) product (Lee et al., 2002) was created by the U.S. Navy Research Lab (NRL). For their real-time TC products, see http://www.nrlmry.navy.mil/TC.html (Hawkins et al., 2001; Hawkins & Velden, 2011). The 37color product made it possible to visualize both the emission and ice-scattering signals at the same time through a single image. The product composited three T_B in the 37 GHz channel, including the vertically (V37) and horizontally polarized T_B (H37), and PCT (PCT37). As mentioned in Kieper and Jiang (2012, KJ12 hereafter), "the ocean surface appears cold in V37 and H37, similar to ice-scattering in deep convection, which also appears cold in both V37 and H37." To correct this ambiguity, the PCT37 is defined by Grody (1993) as

$$\mathrm{PCT37} = 2.18\times\mathrm{V37}–1.18\times\mathrm{H37} = \mathrm{V37} + 1.18\times(\mathrm{V37} - \mathrm{H37}) \quad (1)$$

This relationship essentially makes PCT37 equal to V37 plus 1.18 times the difference between V37 and H37. This correction was done based on an understanding that emissivities of ocean water are a strong function of polarization for the slant viewing angle of satellite passive microwave sensors. V37 and H37 have a large difference when observing the cloud-free ocean. The difference could be as large as 50 K according to Spencer (1986). Therefore, a large polarization correction results in PCT37 values of sea surface ranging between 270 and 300 K, much warmer than their corresponding V37 values, which are usually less than 245 K (see Table 1). The polarization effect of liquid raindrops, either spherical or aspherical, is very small. The difference between V37 and H37 for warm rain or liquid clouds is less than 5 K according to the simulation results of Wu and Weinman (1984). However, for nonraining liquid clouds or light warm rain, the cloud or rain layer is not thick enough to obscure the radiometrically cold and highly polarized ocean surface completely (Spencer, 1986). Therefore, the polarization correction for liquid clouds and warm rain ranges from near zero for thick rain layer to about 30 K for thin cloud or rain layer. The resulting PCT values are fairly warm as well, similar to the ocean surface's PCT, ranging between about 275 and 290 K as summarized in Table 1. Due to largely random orientation and nonflat habits of ice particles, the difference between V37 and H37 of deep convective clouds is relatively small. For aspherical ice particles, the difference is about 15 K (Wu & Weinman, 1984). For deep precipitating clouds with ice particles in random orientations, PCT37 values are nearly equal to their V37 values due to near-zero polarization effect. PCT37 values for precipitating clouds with ice could drop as cold as 69 K in a thunderstorm over land (Zipser et al., 2006) and as warm as 275 K depending on how much emission from liquid water occurs below the freezing level and how much scattering from ice occurs above it.

Based on the understanding of radiative transfer described above and the summary in Table 1, we can say that, in general, the PCT37 is very sensitive to ice scattering and can be used to distinguish ice scattering from either ocean surface or liquid clouds/warm rain. But it is almost impossible to use PCT37 to differentiate between ocean surface and liquid clouds/warm rain because both of these features are very warm as measured by PCT37. On the other hand, after ice has been ruled out by using PCT37 (i.e., when PCT37 is warmer than 270–275 K), H37 and V37 can be used to distinguish ocean surface versus liquid cloud/warm rain.

The 37color product combines the signals of emission from V37/H37 and ice scattering from PCT37 into a false-color display product (Lee et al., 2002). The false-color display technique has been used in the meteorology field for a few decades for visualizing IR (Colwell, 1983; Short et al., 1976), water vapor (Petersen et al., 1984), and passive microwave (SSM/I; Negri et al., 1989) satellite observations. The technique usually combines three spectral bands, that is, red, green, and blue (RGB), as in the true-color images seen by human

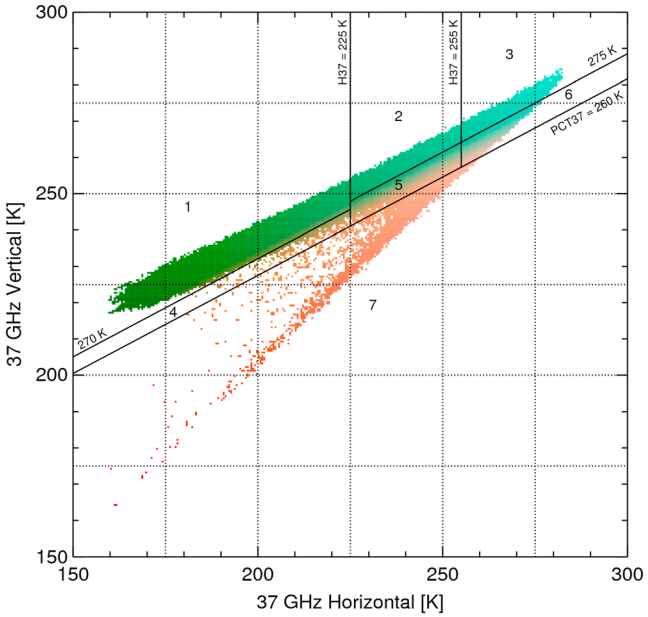

Figure 1. Scatter plot of colors in the NRL 37color product as a function of H37 and V37 derived from the inner region of TCs directly observed by the TRMM PR and TMI during 1998–2011. Seven color regions are defined as in Table 2. Constant PCT37's of 260, 270, and 275 K are shown as the tilted solid black lines.

eyes into a false-color image. In the 37color product, an RGB color composite method is used in constructing the 37color images. PCT37, V37, and H37 values are displayed into RGB guns, respectively. See Lee et al. (2002) for more details of this technique. The quantitative information is sacrificed in the resulting color composite image. But by using H37, V37, and PCT37 in the same image, the product can qualitatively distinguish ocean surface, liquid cloud/rain, and ice. According to Lee et al. (2002), "The sea surface in the color product appears green. Deep convection, including the portion of the eyewall mentioned above, appears pink. Low-level water clouds and rain appear cyan." Table 1 summarizes the features in the 37color product and corresponding PCT37, V37, and H37 ranges as observed in TCs (see Figure 1 and more details in section 3). An TC example of the 37color product and PCT37, V37, and H37 fields is shown in Figure 2, along with a vertical cross section as observed by the TRMM Precipitation Radar (PR) in Figure 3. More detailed explanations of Figures 2 and 3 can be found in section 3.

Many TCs experience one or more rapid intensification (RI) events during their lifetime. Predicting these events is one of the greatest challenges facing TC forecasters (Rappaport & Coauthors, 2009). Previous studies have linked TC intensification with both axisymmetric (Nolan & Grasso, 2003) and asymmetric (Montgomery et al., 2006) processes in the inner core. Using the 37color product, KJ12 identified a cyan + pink ring up to 150-km radius from the TC center, which was found to be a good predictor of RI. A subjective RI forecast method was proposed by KJ12 by using the 37-GHz ring with the environmental-based RI Index (Kaplan et al., 2010). By examining all 28 RI events in the Atlantic basin during 2003–2007, the method correctly captured 21 events and produced only two false alarms. The method was tested in real time in 2008 Atlantic hurricane season by sending forecasts to the "Tropical-storms" e-mail list. This test was remarkably successful, correctly predicting all 2008 Atlantic RI cases with no false alarms. In 2011–2013, an automatic 37-GHz ring RI index was developed under the National Oceanic and Atmospheric Administration Joint Hurricane Testbed program. It has been in real-time testing mode since 2012, and the results are very promising (Jiang et al., 2014, 2015). However, an immediate question raised from the success of the 37-GHz ring forecast method is *"what do the cyan and pink colors in the 37color product indicate, i.e., what type of cloud or precipitation is in these color pixels?"* Based on Table 1 and the theory described above, cyan represents liquid emission and pink represents ice scattering. But we often observe hybrid pink colors on 37color TC images as either green-pink or cyan-pink. We also observe variability in the brightness of cyan ranging from "weak" green-cyan to strong "bright" cyan. Lee et al. (2002) designated pink as deep convection, but our experience indicates that this is only true for isolated pure pink regions. Hybrid pink regions resemble broader regions of stratiform precipitation. Therefore, more careful examinations are needed in order to quantitatively interpret the true meaning of different colors in the 37color product.

The TRMM satellite provided simultaneous passive microwave and radar measurements for global TCs during 1997–2014. Tao and Jiang (2015, hereafter TJ15) used the 14-year TRMM M TMI and PR data to examine the relationship between the 37 GHz cyan + pink ring and RI. They found that 80% (112 out of 139) PR overpasses of global RI storms during 1998–2011 have a ring (see TJ15, Table 2). This finding is generally consistent with KJ12's finding of 75% probability of detection for Atlantic TCs during 2003–2007. By defining precipitation as PR reflectivity ≥20 dBZ at any vertical level, TJ15's Figure 18 showed a 95% closed ring of precipitation for all RI overpasses with a 37-GHz ring. They further concluded that the cyan + pink ring is mainly precipitative, mostly contributed by shallow and moderate precipitation. However, TJ15 took the cyan + pink regions as a whole and did not separate different color regions.

The goal of this study is to develop a new precipitation type classification method for TCs from 37 GHz observations by conducting a more careful examination of different colors in the 37color product. Separating convective and stratiform precipitation types is very important for passive microwave rainfall retrievals. Currently, rain type classification algorithms are available for ground-based radar observations (Steiner et al., 1995) and

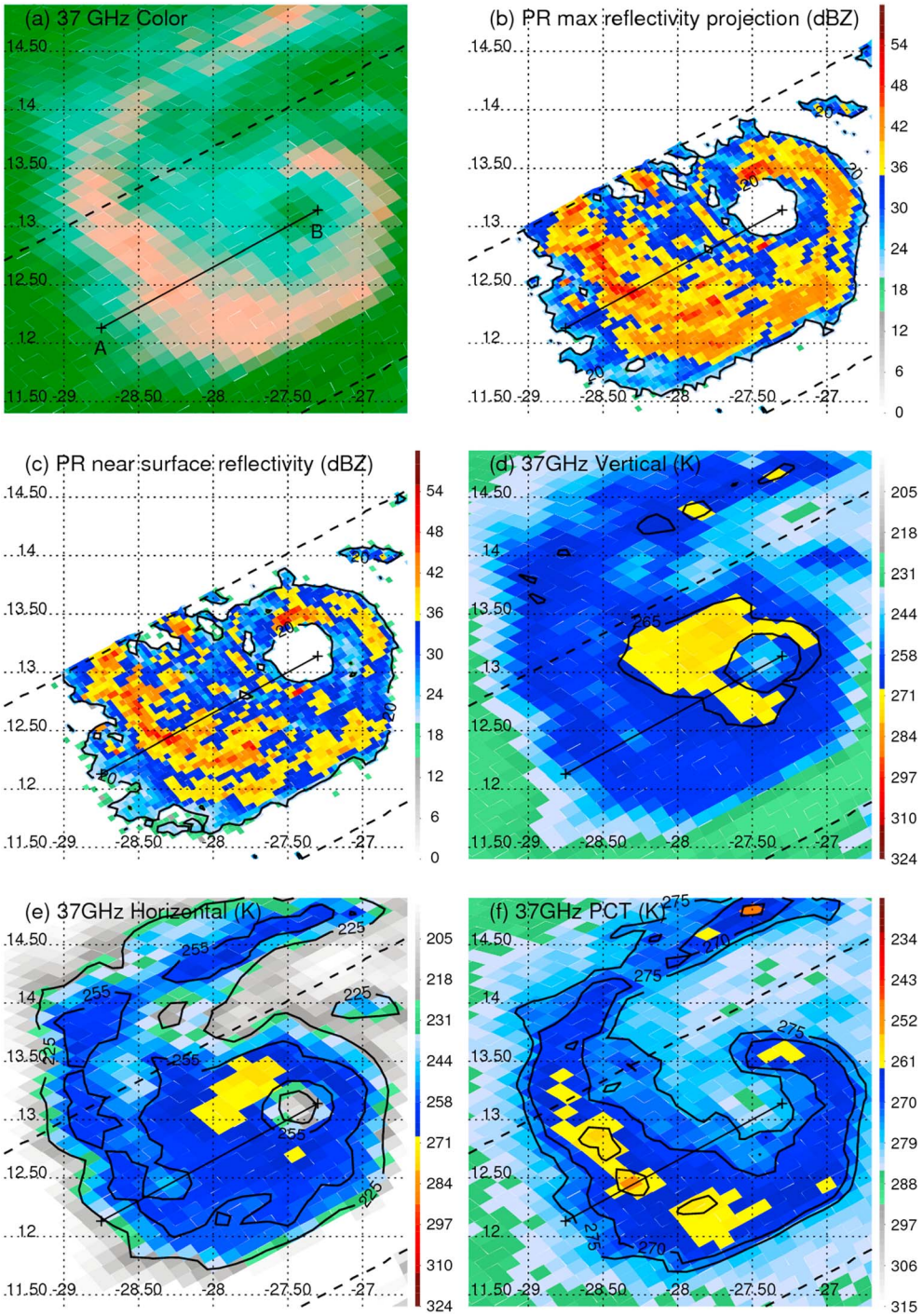

Figure 2. Horizontal plan view of (a) 37color, (b) PR maximum reflectivity projection (dBZ), (c) PR near-surface reflectivity (dBZ), (d) 37 GHz vertically polarized Tb (V37, K), (e) 37 GHz horizontally polarized Tb (H37, K), and (f) 37 GHz polarization corrected Tb (PCT37, K) observed by TRMM for Hurricane Danielle 2004 at 15:27 UTC 14 August 2004. About 225 and 255 K contours of H37; 265 K contour of V37; 260, 270, and 275 K contours of PCT37; and 20 dBZ contour of PR maximum reflectivity projection and PR near-surface reflectivity are indicated in corresponding panels. The dashed line in (a)–(f) is the edge of the PR swath.

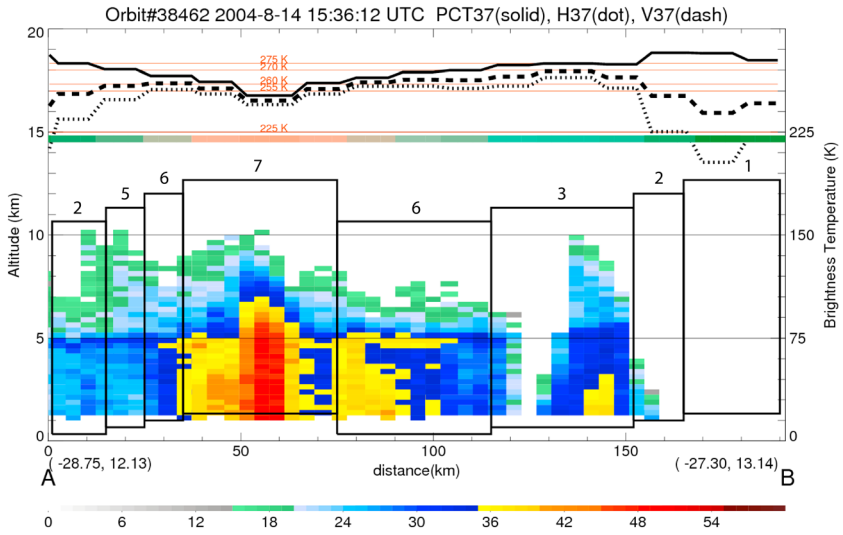

Figure 3. Vertical cross section of PR reflectivity (dBZ in color) along the line in each panel of Figure 2 across Hurricane Danielle's inner core region. Values of H37, V37, and PCT37 along the line are indicated as dot, dash, and solid black curves, respectively. About 225, 255, 260, 270, and 275 K T_B thresholds are indicated as red straight lines. The corresponding color of the 37color product for each pixel is shown as a thick strip right below the T_B = 225 K line. The latitudes and longitudes of the starting and ending points of the line along which the cross section is made are indicated in the bottom right and left corners of *x* axis.

satellite radar observations such as the TRMM 2A23 (Awaka et al., 2009). The 37 GHz emission signature was used in a rain/no-rain classification (Kida et al., 2009) and a convective/stratiform separation algorithm using the combination of 19, 37, and 85 GHz data (Hong et al., 1999). In this study, we will use the simultaneous TRMM PR and TMI 37 GHz data to investigate the vertical distributions of PR reflectivities in different color regions in the 37color product in TCs, with a goal of developing a precipitation type classification method using both the emission and ice-scattering signature of 37 GHz observations. Section 2 presents the data and methodology used in this study. Section 3 describes the development of the 37 GHz precipitation type classification method for TCs. Section 4 discusses the time evolution of different precipitation types as identified by the 37color product in various stages of RI events. Conclusions are given in section 5.

2. Data and Methodology

The 14-year (1998–2011) TRMM PR and TMI data set of global TCs used in this study is the same as in TJ15. The data set includes 1139 TRMM PR/TMI overpasses with 139 of them being defined as RI overpasses (future 24-hr intensity increase ≥30 kt; Kaplan & DeMaria, 2003). Since storms that have already attained major hurricane strength rarely undergo RI, the data set only contains overpasses with storms in the categories of tropical storm and category 1 and 2 hurricanes, or storms with maximum wind between 18 and 49 m/s according to the Saffir-Simpson Hurricane Wind Scale. The TC center was first determined by linearly interpolating from the National Hurricane Center and Joint Typhoon Warning Center best-track storm center location, and then was adjusted based on the PR or TMI 37 GHz images (Zagrodnik & Jiang, 2014; TJ15). No TCs can be captured by PR completely due to its narrow swath width (215 and 247 km before and after the satellite boost in 2001, respectively). As in Zagrodnik and Jiang (2014), all the PR overpasses were screened subjectively to make sure that at least 75% of the TC inner core region was captured by the PR. See TJ15 for more details of the data set.

The TRMM PR operates at the 13.8-GHz frequency channel. It observes three-dimensional reflectivities with a minimum detectable signal of about 17 dBZ. We use version 7 of the PR 2A25 algorithm reflectivity (Iguchi et al., 2009), which has a horizontal resolution of approximately 4 km × 4 km before boost and 5 km × 5 km after boost and a 250 m vertical resolution at nadir. The collocation of PR and TMI data is provided in the TRMM Precipitation Feature database (Liu et al., 2008). As mentioned in Liu et al. (2008), "The PR scans through nadir, but the TMI scans conically at 52° slant angle. When there are hydrometeors at high altitude, the TMI microwave scattering signal would appear as from the nearby surface because of the 52° slant angle."

Table 2
Seven Color Regions and Their Corresponding Brightness Temperature Ranges as Illustrated in Figure 1

Precipitation type	Region	Definition (T_B in K)	No. of total pixels	No. of all precipitating pixels	% of pixels in the region that are precipitating
Precipitation-free	1 (green)	PCT37 $>$ 270 and H37 $<$ 225	466,460 (56%)	113,203 (25%)	24
Shallow convection or weak stratiform precipitation	2 (weak cyan)	PCT37 $\geq$ 275 and 225 $\leq$ H37 $<$ 255	116,083 (14%)	97,067 (21%)	84
Shallow convection	3 (bright cyan)	PCT37 $\geq$ 275 and H37 $\geq$ 255	38,548 (5%)	37,697 (8%)	98
Stratiform precipitation	4 (green/pink)	260 $<$ PCT37 $\leq$ 270 and H37 $<$ 225	487 (0%)	477 (0%)	99
	5 (weak cyan/pink)	260 $<$ PCT37 $<$ 275 and 225 $\leq$ H37 $<$ 255	73,959 (9%)	73,114 (16%)	99
	6 (bright cyan/pink)	260 $<$ PCT37 $<$ 275 and H37 $\geq$ 255	125,440 (15%)	125,413 (28%)	100
Deep convection	7 (pure pink)	PCT37 $\leq$ 260	8,105 (1%)	8.104 (2%)	100
Total			829,082 (100%)	455,075 (100%)	55

Note. The numbers (percentages) of total pixels and precipitating pixels and % of precipitating pixels for each color region from the same data set as Figure 1 are also indicated.

To correct this parallax effect and to "collocate better with the nadir observations, the TMI data coordinates are moved backward (or forward depending on the orientation of the satellite) for one scan when the PR echo top height $>$ 5 km and the path integrated attenuation $>$ 0.4 dBZ." The TMI 37 GHz brightness temperature data is stored in about 13.0 km $\times$ 7.3 km irregular grid before boost and 13.0 km $\times$ 8.3 km grid after boost. Using the elliptical shape of the TMI footprint, the PR pixel centers that fall within that ellipse are assigned to each respective TMI pixel. Because of the overlap in footprint between adjacent TMI pixels, some PR pixels are assigned to two adjacent TMI pixels. According to the horizontal resolution difference, each TMI 37 GHz pixel usually corresponds to 5–8 PR pixels depending on their geophysical location.

Theoretically, to match PR with 37 GHz observations, a weighting function should be applied to compute one radar profile from the 5–8 PR pixels corresponding to each 37 GHz pixel. However, it requires a complicated microwave sensor simulation in order to get the accurate weighting function. To simplify the problem, in this statistical study, we only analyze the maximum PR profile derived from the 5–8 PR pixels corresponding to each 37 GHz pixel. The maximum PR reflectivity profile for each 37 GHz pixel is obtained by taking the maximum reflectivity at each vertical level from the corresponding 5–8 PR profiles. This approach fits our purpose well because our main research goal is not to calculate the accurate radar reflectivity corresponding to each 37 GHz pixel. Instead, we aim to find out what type of cloud or precipitation is represented by different colors of 37color images.

3. Classification Method Development

Figure 1 presents the scatter plot of colors in the NRL 37color product as a function of H37 and V37 derived from the inner region (within 250 km from the storm center) of TCs directly observed by the TRMM PR and TMI during 1998–2011. The brightness temperatures form an arrowhead shape. The top boundary of the arrowhead is almost parallel to the lines of constant PCT37 because the PCT is empirically derived using the linear difference in liquid water emissivity between 37H and 37V that is represented by the upper boundary of observed 37 GHz T_B values in Figure 1 (Spencer et al., 1989). The lower boundary of the arrowhead has a slope of 1, which is the case for spherical raindrops and spherical ice particles that have equal 37H and 37V values. The exact values of any given point in the pink and cyan areas depend primarily on the relative influence of emissivity by liquid hydrometeors and scattering by frozen hydrometeors. The spread in the green region may depend on other factors such as sea surface temperature, sea spray, and atmospheric clouds/water vapor. When precipitation is occurring, these secondary factors are overwhelmed by the strong emission and scattering of precipitation-sized hydrometeors.

Seven regions in Figure 1 with different 37color shades (corresponding to five precipitation types) are defined, and the T_B range for each type is shown in Table 2. The T_B thresholds are carefully chosen based on the corresponding PR reflectivity profiles of each region in order to optimally separate precipitation-free, shallow precipitation/convection, stratiform precipitation, and deep convection. Interestingly, different precipitation types correspond to different color shades in the 37color product. This is because the 37color

product design allows the qualitative influence of emission and scattering for any given color to be easily deduced from Figure 1. Table 2 lists the number of total TMI 37 GHz pixels for each region from the inner region of TCs observed by the 1,139 TRMM TMI/PR overpasses during 1998–2011. As described in section 2, we match each 37 GHz pixel with the maximum PR reflectivity profile from the corresponding 5–8 PR profiles. A pixel is defined as a precipitating pixel if its corresponding maximum PR reflectivity profile has at least one value reaching 17 dBZ (which is the PR's minimum detectable signal) from any vertical level. The number and percentage of precipitating pixels from each region are also listed in Table 2. When we separate different regions, we first try to classify regions with 100% precipitating pixels. These regions are most important for precipitation type identification since they are not contaminated with nonprecipitating clouds and sea surface.

From Table 2 and Figure 1, there are five regions with nearly 100% precipitating pixels, including region 3 (bright cyan in the 37color product, 98% precipitating pixels), 4 (green/pink, 98%), 5 (weak cyan/pink, 99%), 6 (bright cyan/pink, 100%), and 7 (pure pink, 100%). All four pink regions, including pure pink (which can be called as bright pink due to its look, but we call it pure pink in the following text) and hybrid pink (green/pink, weak cyan/pink, and bright cyan/pink), have low PCT37 values, indicating precipitation with ice above the melting level. The bright cyan region is also precipitative, but with high PCT37 and H37 values, indicating precipitation without or with little ice. Eighty-four percent of pixels in the weak cyan region (region 2) are precipitating pixels, while only 24% of the pixels in the green region (region 1) are precipitating. Interestingly, pure pink pixels represent only 1% of the total pixels in the inner region of TCs, and 2% of total precipitating pixels (Table 2). The bright cyan, weak cyan/pink, weak cyan, green, and bright cyan/pink represent 8%, 16%, 21%, 25%, and 28% of precipitating pixels, respectively.

Please note that sensitivity tests have been done to choose the T_B thresholds in Figure 1 and Table 2. It was very hard to decide visually between 270 and 275 K on which one is better for colors between hybrid pink and no pink. We eventually choose 275 K as the threshold because we would like to have a physically meaningful separation. As we tested initially, using PCT37 $\geq$ 270 K and H37 $\geq$ 255 K to define the bright cyan region (region 3 in Figure 1) will contaminate shallow convection with a lot of stratiform precipitation. Only when we changed the threshold to PCT37 $\geq$ 275 K and H37 $\geq$ 255 K, were we able to isolate shallow convection from stratiform rain fairly well. Using PCT37 $\geq$ 275 K to separate pink and no pink is even justified visually by the example shown in Figure 2 below. The 275 K contour of PCT37 in Figure 2f does include some hybrid pink (with a faded shade of pink over cyan or green) regions that beyond the 270 K contour. One example of hybrid pink region with 270 $\leq$ PCT37 $\leq$ 275 K is around 12°N and 28.5°W in Figures 2a and 2f. The other example is the small area on the tail of the rainband in the square of 28–28.5°W and 14–14.5°N, and between 27.75–28.25°W and 14.5–15°N on Figures 2a and 2f.

Table 2 shows that region 1 (green) is precipitation-free, region 2 (weak cyan) is shallow convection or stratiform precipitation, region 3 (bright cyan) is shallow convection, regions 4–6 (hybrid pink) are stratiform precipitation, and region 7 (pure pink) is deep convection. Next, we will illustrate and justify the precipitation type classification in Table 2 by using one case (Figures 2 and 3) and some statistical analysis (Figure 4).

Figures 2 and 3 illustrate an example of 37 GHz and radar images in the inner core region of Hurricane Danielle (2004) observed by a TRMM overpass at 15:27 UTC 14 August 2004. At the time of this observation, Danielle was in the tropical storm with a maximum sustained wind speed of 51 kt (interpolated from the best track data). In the following 24 hr, Danielle rapidly intensified to category 1 hurricane with 24-hr intensity increase of 33 kt. The 37color product of this TRMM overpass showed a cyan + pink ring pattern around the storm center (Figure 2a), which satisfied the criteria of KJ12 to be forecast as an RI case. The eye is obviously seen in the 37color panel (Figure 2a) as a round-shape green region. Surrounding the eye, a cyan and pink ring pattern is clearly seen (note that if you are reading a printed copy of the figure, the cyan color might not be as clear as in the electronic copy viewed from a computer screen). The 225 K contour of H37 (Figure 2e) outlines the eye region and the whole cloud/precipitation pattern of the storm, while the 255 K contour of H37 and 265 K contour of V37 (Figure 2d) could be used to roughly differentiate bright cyan and weak cyan. The 275 and 270 K contours of PCT37 (Figure 2f) generally outline the ice-scattering region with either hybrid or pure pink color shown in the 37color image (Figure 2a), similar as shown in Figure 1. The 260 K contour of PCT37 indicates pure pink color regions in Figure 2a. The PR maximum reflectivity projection (Figure 2b) is the maximum reflectivity value in each vertical column as observed by the PR.

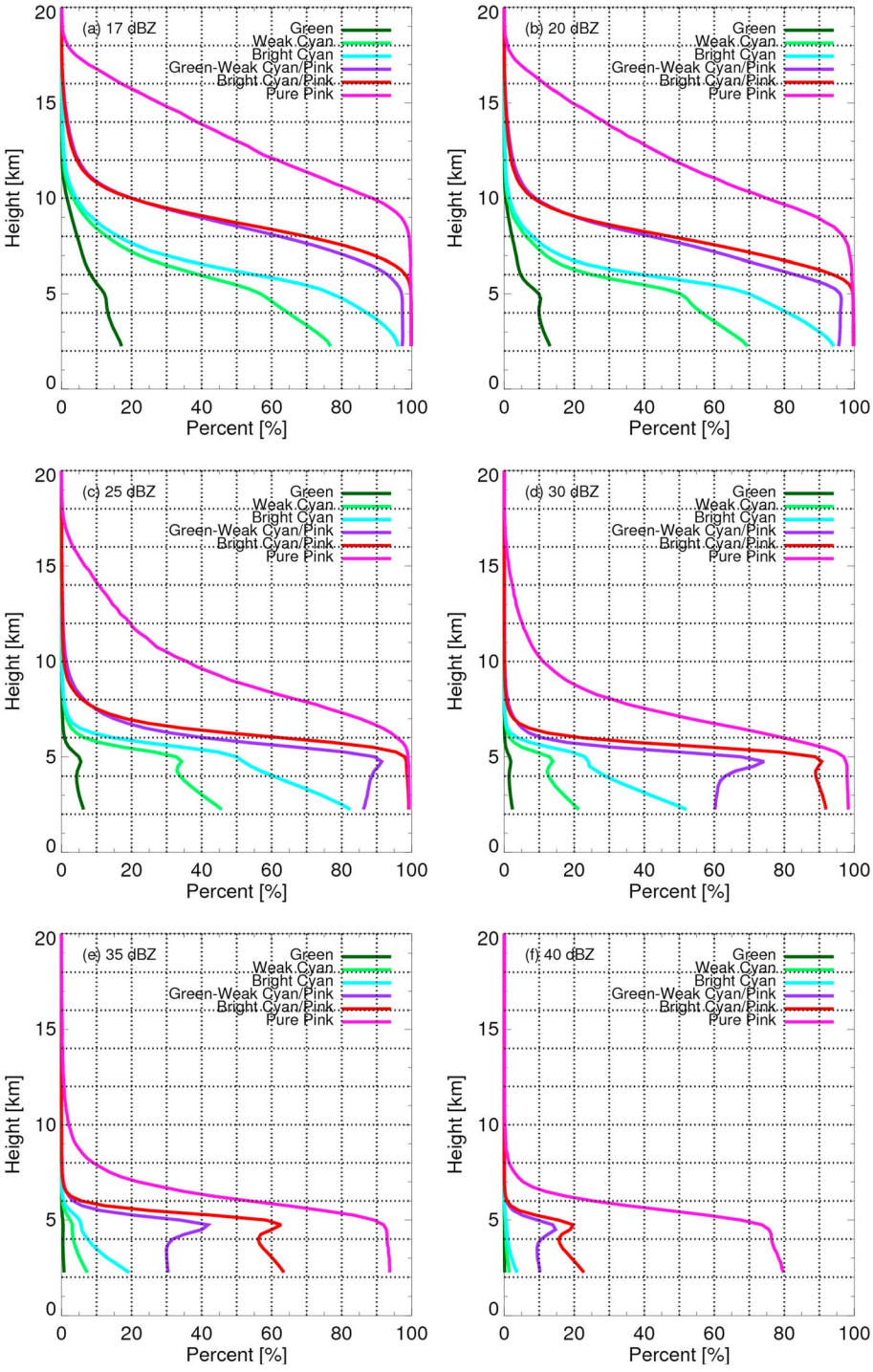

Figure 4. The vertical profile of percentage of PR reflectivity: (a) ≥17 dBZ, (b) 20 dBZ, (c) 25 dBZ, (d) 30 dBZ, (e) 35 dBZ, and (f) 40 dBZ for all the maximum PR profiles corresponding to 37 GHz pixels in different color regions using the same data set as in Table 2.

Radar reflectivity ≥17–20 dBZ is a good indicator of rain. Comparing Figures 2b and 2c with Figure 2e, we can see that the 225 K contour of H37 roughly matches the 20 dBZ contour of the PR maximum reflectivity projection (Figure 2b) and near-surface radar reflectivity (Figure 2c), except that the H37 225 K contour covers a bit more area on the edge (for example, the eye area in H37 is smaller than the PR near-surface reflectivity). This could be due to (1) the footprint of TMI at 37 GHz that is about 5 times larger than PR or

(2) there are some low-level clouds with very small liquid particles that can be seen by 37 GHz but cannot be detected by the TRMM PR.

Figure 3 shows the vertical cross section of PR reflectivity along the line indicated in each panel of Figure 2 across the inner core region of Hurricane Danielle. The cross section is shown from southwest to northeast along the line. The corresponding color of the 37color product for each pixel is shown as a thick strip below the T_B = 225 K line. From Figure 3, we can see that the cross section starts with a light precipitation region corresponding to distance (*x* axis) between ~1 and ~15 km (the first box on Figure 3) from the cross section line's starting point (28.75°W, 12.13°N). In this segment, PCT37 is equal or warmer than 275 K and H37 is between 225 and 255 K. As defined in Table 2, this segment is region 2 with weak cyan color on the 37color product and the precipitation type should be either shallow convection or stratiform precipitation. PR reflectivity shows that this segment is mainly weak precipitation echo with some ice above the freezing level, which is about 5 km. There is a very weak bright-band signature indicating possible stratiform rain type.

The next segment of Figure 3 is between 15 and 25 km distance from the starting point. This segment is region 5 (weak cyan/pink) as defined in Table 2 and corresponds to 260 K $<$ PCT37 $<$ 275 K and 225 K $\leq$ H37 $<$ 255 K. The PR reflectivity cross section shows a typical stratiform rain type with the echo top reaching 10 km height and a distinctive bright-band feature near the freezing level. The third segment is between 25 and 35 km. This segment is region 6 (bright cyan/pink) as defined in Table 2 with 260 K $<$ PCT37 $<$ 275 K and H37 $\geq$ 255 K. The vertical radar reflectivity distribution of this segment is very similar to that of the previous segment, except with greater dBZ values below the freezing level. The fourth segment is between 35 and 75 km. This segment is region 7 (pure pink) as defined in Table 2 with PCT37 $\leq$ 260 K. The vertical radar reflectivity distribution shows a typical deep convective cell feature with the echo top reaching 10 km and the near-surface reflectivity as high as ~50 dBZ. The segment between 75 and 115 km is region 6 (bright cyan/pink) again as the third segment, with vertical radar reflectivity showing a typical stratiform precipitation type. The sixth segment between 115 and 152 km is region 3 (bright cyan color) as defined in Table 2 with PCT37 $\geq$ 275 K and H37 $\geq$ 255 K. The vertical radar reflectivity of the bright cyan region shows a shallow convective feature with higher reflectivity values near the surface. However, this is unrepresentative example of region 3 with an echo top height reaching 10 km. As seen later in Figures 4 and 5, majority of the radar pixels in region 3 reaches only 8 km or even lower. In this study, we define this type of pixels as shallow convection (Table 2). Note that this is slightly different from the shallow convection (or shallow cumuli) in the trimodal distribution identified by Johnson et al. (1999), in which the echo top height must be lower than the freezing level. However, due to the unique TC environment with strong horizontal winds, some ice could be advected from other regions to the top of the shallow convection, which will make some of the bright cyan pixels have a higher than normal echo top.

The next segment is short, between 152 and 165 km, including only one 37 GHz pixel. It is region 2 (weak cyan color) again as defined in Table 2 with PCT37 $\geq$ 275 K and 225 K $\leq$ H37 $<$ 255 K. Within this 37 GHz pixel, there should be 5–8 corresponding PR pixels, in which only two PR pixels have a weak and shallow radar echo and the rest has no radar echo. The last segment is between 165 and 190 km. The 37color product shows a green color in this segment, corresponding to the hurricane eye region without any radar echo with PCT37 $>$ 270 K and H37 $<$ 225 K. This is precipitation-free (region 1) as defined in Table 2.

To further examine the percentage of precipitating pixels at different vertical levels, Figure 4 shows the vertical profiles of percentage of PR reflectivity $\geq$17, 20, 25, 30, 35, and 40 dBZ for all the maximum PR profiles corresponding to 37 GHz pixels in different color regions using the same data set as in Table 2. A similar type of analysis was done by Zawislak and Zipser (2014). Figure 4a shows that pure pink (region 7) has the highest percentages of precipitating pixels (reflectivity $\geq$17 dBZ) in all levels, followed by bright cyan/pink (region 6), green-weak cyan/pink (regions 4–5), bright cyan (region 3), weak cyan (region 2), and green (region 1) regions in decreasing order. All pure and hybrid pink regions (regions 4–7) have 100% or nearly 100% of precipitating pixels below 5 km. The bright cyan region (region 3) has about 98% of precipitating pixels near surface. Compared with Table 2, this indicates that all the precipitating pixels in the pink region (regions 4–7) and bright cyan region (region 3) are raining near surface, not just aloft. The weak cyan (region 2) and green (region 1) regions have about 78% and 18% of their pixels raining near surface, respectively, which are 6% smaller than the percentages of total precipitating pixels for these two regions in Table 2. This indicates

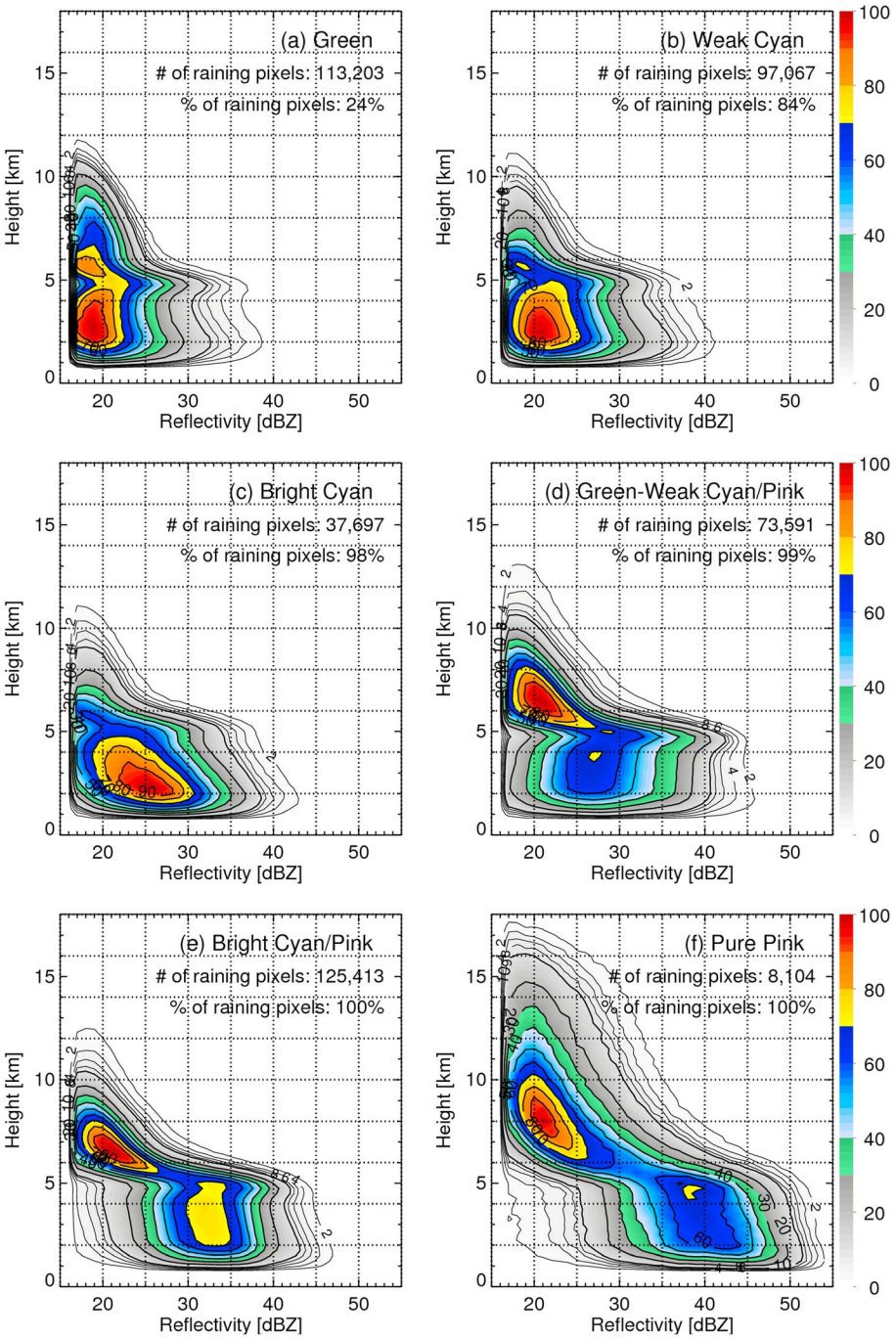

Figure 5. CFADs of the maximum PR reflectivity profile within each TMI 37 GHz pixel in different color regions as defined in Table 2 and Figure 1: (a) region 1: Green, (b) region 2: weak cyan, (c) region 3: bright cyan, (d) regions 4 and 5: green/pink and weak cyan/pink, (e) region 6: bright cyan/pink, and (f) region 7: pure pink. Contours represent the frequency occurrence relative to the maximum frequency bin (1 dB in size, 250 m in height). Only precipitating pixels (see Table 2 and text for details) are used to generate the CFADs.

that about 6% of both weak cyan (region 2) and green (region 1) regions contain anvil pixel raining aloft only. The percentage of precipitating pixels decreases rapidly with height for all different color regions. At 10 km height, there are 90, 20, 20, 5, 5, and 2% of precipitating pixels for pure pink (region 7), bright cyan/pink (region 6), green-weak cyan/pink (region 4–5), bright cyan (region 3), weak cyan (region 2), and green (region 1) regions, respectively.

When increasing the reflectivity threshold to higher values, the percentages decrease accordingly for each color region. The pure pink and bright cyan/pink regions have 100% or nearly 100% of pixels reaching 20 dBZ (Figure 4b) and even 25 dBZ (Figure 4c) below 5 km. Recall in Table 2 that the only difference between pure pink and hybrid pink is the PCT37 $\leq$ 260 K threshold for pure pink. But the pure pink region only has 98%, 93%, and 73% of pixels reaching 30 (Figure 4d), 35 (Figure 4e), and 40 dBZ (Figure 4f), respectively, below 5 km. At the surface, the bright cyan/pink region has 91%, 62%, and 22% of pixels reaching 30 (Figure 4d), 35 (Figure 4e), and 40 dBZ (Figure 4f), respectively. The percentage of pixels greater than a given reflectivity threshold decreases for different color regions in the following order from the highest to lowest: pure pink, bright cyan/pink, green-weak cyan/pink, bright cyan, weak cyan, and green regions. The 90th percentile echo top height at a given reflectivity threshold decreases in the same order too. For example, the 90th percentile of the 20 dBZ echo top height of the pure pink region reaches as high as 16 km, much higher than those of the three hybrid pink regions (10 km) and the green (4 km), weak cyan (7 km), and bright cyan regions (7.5 km). The 90th percentile of the 40 dBZ echo top height of the pure pink region reaches as high as 6.6 km, which is higher than those of the three hybrid pink regions (5 km).

Figure 5 provides the contoured frequency by altitude diagrams (CFADs; Yuter & Houze, 1995) of the maximum PR reflectivity profile within each 37 GHz pixel for all precipitating pixels for different regions as defined in Table 2 and Figure 1 from the inner region of TCs observed by the 1,139 TRMM TMI/PR overpasses during 1998–2011. The "CFADs are normalized relative to their respective maximum frequency to account for different sample sizes", as in Hence and Houze Jr (2011) and Hence and Houze Jr. (2012). Distinct differences are seen in the CFADs from different color regions. The CFAD for precipitating pixels in region 1 (green color in the 37color product; Figure 5a) has very weak low-level echoes with a peak centered at 18–19 dBZ indicating very light rain (such as drizzle or small isolated showers) near the surface. It also has a distinctive bright-band feature around 5 km, indicating stratiform rain type. The reflectivities decrease with height above the freezing level, with the 50% frequency reaching about 8.5 km and outlier distribution reaching nearly 12 km height. Note that 76% of these green pixels have no radar echo.

The CFAD for precipitating pixels in the weak cyan region (Figure 5b) shows a bottom-heavy pattern with most of the distribution packed below the freezing level with a peak centered at 20–22 dBZ close to the surface. A less distinctive bright-band signature is seen, with the 50% frequency reaching nearly 6.5 km. Reflectivities below the freezing level slightly increase downward, likely a product of warm-rain processes. The bright cyan region (Figure 5c) presents a more distinct bottom-heavy pattern than the weak cyan region with a significant increase of reflectivity downward with a broad 50% frequency distribution ranging between 17 and 33 dBZ at near surface (peaked at 25 dBZ). Warm-rain processes (i.e., collision-coalescence) are most likely responsible for the significant increase in reflectivity with decreasing height below the bright band in this region (Schumacher & Houze Jr., 2003). The *Glossary of Meteorology* (Glickman, 2000) defines the warm rain process as "growth by collision-coalescence." The glossary also mentioned that the warm rain process "occurs in clouds having sufficient liquid water, updraft, and lifetime to sustain collision-coalescence" and "is found to be active in both shallow and deep convection." Thus, the warm rain process here is more likely associated with convective clouds. Note that warm rain process does not require or imply an absence of frozen condensate aloft. Instead, warm rain can coexist with ice scattering above, similarly to that shown in Figures 4b and 4c.

The CFADs for the green-weak cyan/pink (Figure 5d; note that this is for the combination of regions 4 and 5 in Figure 1) and bright cyan/pink regions (Figure 5e) are both showing the typical stratiform distribution with a strong bright-band feature, but the radar reflectivity intensities are quite different. In the green-weak cyan/pink (Figure 5d), the below-freezing-level peak is around 28 dBZ. In the bright cyan/pink region (Figure 5e), the below-freezing-level peak is shifted to even stronger reflectivity values, that is, between 30 and 35 dBZ. Compared with the weak cyan region (Figure 5b), stronger reflectivities are observed at higher altitude above the freezing level in the green-weak cyan/pink and bright cyan/pink regions, with a peak centered at about 19–24 dBZ between 5 and 6 km.

Houze Jr et al. (2015) found a type of precipitation in many tropical and subtropical precipitation systems, which they define as "weak cellular broad stratiform regions." Due to the existence of bright bands, these regions are classified as stratiform by the TRMM 2A23 algorithm (Awaka et al., 2009) despite the cellular nature of the reflectivity field (see Figures 11 and 12 of Houze Jr et al., 2015). Houze Jr et al. (2015) speculated

"that such echoes may be falsely identified as stratiform" and may be associated with shallow convection. This precipitation type is closely linked with the bright cyan/pink region (Figure 5e) defined in the current study, as this region does have a distinctive bright band (although it is weaker than that in Figure 5d) and a slight increase of reflectivity with decreasing height below the freezing level. Therefore, we speculate that the bright cyan/pink region might include some mixed stratiform and shallow convective precipitation with a bright band above and shallow warm-rain-type convection below. Further research using satellite-based, ground-based, and/or airborne radar data is needed to better understand this coexisting stratiform and shallow convective precipitation type in the complex environment of hurricanes.

The CFAD for the pure pink region (Figure 5f) shows a typical deep convection distribution similar to Hence and Houze Jr's (2011) Figure 2c for convective CFAD in the eyewall. Intense low-level echoes decrease their reflectivity values slowly with increasing height, with a broad greater than 50% frequency distribution ranging from 35 to 45 dBZ with a center peaked at around 40 dBZ. Below 4 km, reflectivities are quite high with the highest reaching 54 dBZ. Above the freezing level, reflectivity values decrease more slowly and intense outliers reach much higher altitude than is seen in Figures 5a, 5d, and 5e. As seen in Table 2, pure pink occupies a very small fraction of the inner region of TCs, only counting for 2% of total precipitating pixels. The relative lack of deep, intense convection in TCs is consistent with previous findings (Cecil et al., 2002; Jiang, 2012; Jiang et al., 2013; Tao & Jiang, 2013; Zagrodnik & Jiang, 2014; TJ15).

4. Time Evolution of 37color Features During Rapid Intensification Events

As mentioned in section 1, the 37 GHz cyan + pink ring was found to be a good indicator of RI (KJ12). Results in section 3 indicate that different 37 GHz color regions defined in this study represent unique precipitation/convective types. It would be interesting to further investigate how the coverage of different 37 GHz color regions (therefore different precipitation/convective types) changes during the evolution of RI events. Tao et al. (2017) developed an approach to define RI events from TC best track data and to stratify each RI event into before RI, during RI, and RI ending periods. As illustrated in their Figure 1, "before RI" is for any time before the onset of an RI event. "During RI" is for the time period between RI onset and 24-hr before RI ends. "RI ending" is the last 24-hr of each RI event. Using this approach, a total of 595 well-observed TMI overpasses is identified to be associated with RI events during 1998–2013 (Tao et al., 2017) and is stratified into different stages of RI events. Figure 6 shows the time evolution of azimuthally averaged percentage coverage of different 37color regions and their combinations as a function of radius from the TC center and time relative to the onset and ending of RI events observed by the 595 TMI overpasses.

In general, obvious changes of precipitation/convection coverage with time are only seen within the inner core region of TCs (radius $<$ 100–150 km). Beyond the 150 km radius, changes are little. Both bright cyan (Figure 6a) and pure pink regions (Figure 6b) have a peak coverage around 45 hr before RI onset. This implies that both shallow convection and deep convection peak about 1.5 days or earlier before the onset of RI, similar as Alvey III et al. (2015). TJ15 proposed a hypothesized sequence of precipitation/convection events associated with RI. In their Figure 13, they mentioned that before RI isolated very deep convection is often observed based on previous RI case studies using aircraft data (Rogers et al., 2015; Stevenson et al., 2014; Susca-Lopata et al., 2015). Figure 6b confirms that this is also true statistically from the TRMM data, but it is still unclear if the deep convection maximum as early as 1.5 days or earlier before RI provides any preconditioning that favors the subsequent RI. The percent coverage of the bright cyan region (shallow convection) decreases gradually between 45 and 3 hr before the onset of RI, then increases gradually starting at 3 hr before RI and peaks again during RI. However, the pure pink region (deep convection) does not increase much until 3 hr after the onset of RI. The maximum percentage of the pure pink region only reaches 3%, indicating again the relatively lack of deep convection in the inner core of TCs. The weak cyan region, containing a mixture of nonprecipitating clouds, shallow convection, stratiform rain, and anvil clouds as shown above, increases as early as 15 hr before RI onset (Figure 6c), levels off till 3 hr after RI onset, and then decreases during RI and RI ending period. A sharp increase of coverage at 3–9 hr before RI is seen when we combined all three hybrid pink (Figure 6d), bright cyan and all four pink (Figure 6e), and all cyan + pink (Figure 6f) regions. As seen in the above section, all three hybrid pink regions are mainly stratiform rain, which covers around 30–55% of the inner core area (Figure 6d). Figure 6e represents all nearly 100% raining regions including both stratiform and convective rains, and Figure 6f represents all mostly precipitating regions by further including

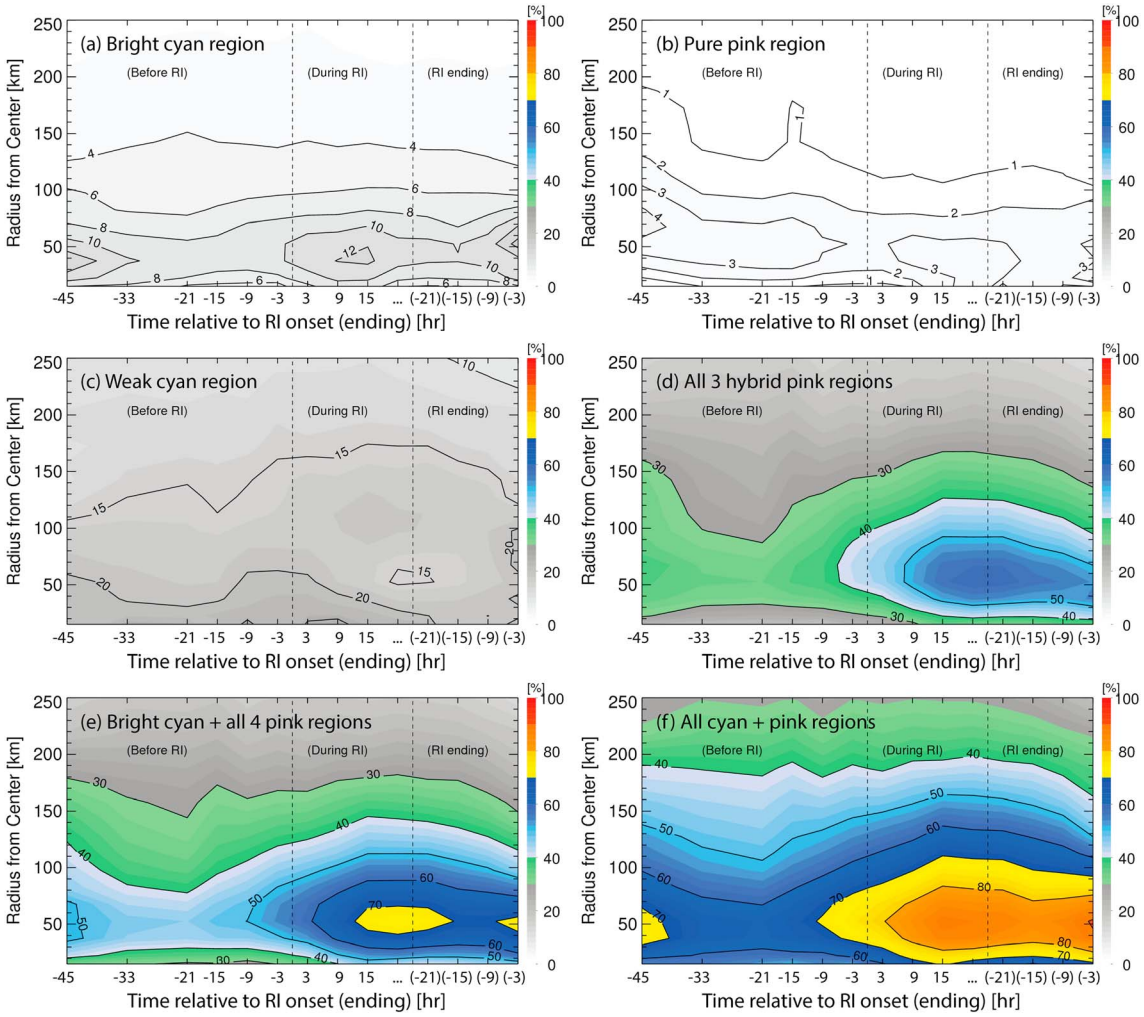

Figure 6. Hovmoller diagrams of azimuthally averaged coverage (%) of (a) bright cyan (region 3), (b) pure pink (region 7), (c) weak cyan (region 2), (d) three hybrid pink (regions 4–6), (e) bright cyan + all four pink (regions 3–7), and (f) all cyan + pink (regions 2–7) regions as defined in Figure 1 and Table 2 as a function of time relative to the onset and ending of RI and distance from the storm center. The vertical dashed lines indicate RI onset and 24 hr before RI ends.

the weak cyan region. The composites in Figures 6d–6f indicate that over 70–80% of the annulus between 40 and 70 km around the storm center is covered by rain, in general, with over 50% covered by hybrid pink (regions 4–6, classified as stratiform rain in this study) during RI. This is consistent with KJ12's cyan + pink ring finding and also indicates that the ring contains mostly rain, consistent with TJ15.

Tao et al. (2017) compared the relative contribution of stratiform and convective precipitation during the evolution of RI events by using the TRMM PR 2A23 (Awaka et al., 2009) rain type product. Same as what we seen here in Figures 6e and 6f, they also found a significant increase of rainfall coverage 3–9 hr prior to the onset of RI and that the increase is mainly contributed by stratiform rain. Our results further indicate that the increase is led by an increase of all three hybrid pink (mainly stratiform rain) regions starting as early as 21–15 hr before RI (Figure 6d), followed by an increase of bright cyan (shallow convection, Figure 6a) starting around 3 hr before RI, and an increase of pure pink (deep convection, Figure 6b) starting around 3 hr after RI onset. Many previous modeling or aircraft-based case studies emphasized the role of deep convection in TC intensification, in general (Hendricks et al., 2004; Rogers et al., 2013), and RI, in particular (Molinari & Vollaro, 2010; Reasor et al., 2009; Rogers et al., 2015; Stevenson et al., 2014; Susca-Lopata et al., 2015). But this study, along with previous satellite-based statistical studies (Zagrodnik & Jiang, 2014, TJ15, Tao et al., 2017), has shown that RI events usually start right after a significant increase of stratiform precipitation and shallow convection. As speculated by Zawislak et al. (2016) and Tao et al. (2017), a minimum of stratiform rain around 21 hr before

RI onset and an increase after 21 hr might be associated with the change of moisture field within the TC. An increase in stratiform precipitation might help provide a necessary condition to activate other processes during RI by gradually moistening the upshear quadrants, which are originally quite dry and usually precipitation-free before RI. However, it is still unclear what processes are crucial in triggering and maintaining RI. Fully addressing this question is beyond the scope of this study but provides directions for future studies.

5. Conclusions

With 14 years of TRMM PR and TMI observations of the inner region of global TCs, precipitation/convection types are classified based on seven color regions corresponding to the 37color product (Lee et al., 2002) defined using 37 GHz T_B including PCT37 and H37. The percentage of precipitating pixels and distribution of vertical radar reflectivity profiles are examined in order to find the dominant type of precipitation/convection contained in different color regions of 37color images. The major findings include the following:

1. The pure pink region is *deep convection* with 100% precipitating pixels near surface and significant ice above the freezing level. Less than 2% of total precipitating pixels in the 1,139 TC overpasses studied are pure pink, indicating the relatively lack of deep, intense convection in the inner region of TCs, consistent with many previous studies.
2. The bright cyan region is mainly shallow convective precipitation with nearly 100% precipitating pixels near surface and little ice above the freezing level.
3. The hybrid pink regions including green/pink, weak cyan/pink, and bright cyan/pink are mainly stratiform precipitation with a distinctive bright band feature. However, the bright cyan/pink region might contain some shallow convection coexisting with the stratiform precipitation.
4. Pixels in the weak cyan region are 16% nonprecipitating and 84% precipitating. The precipitating pixels are either shallow convective or stratiform precipitation. Pixels in the green region are 76% of nonprecipitating and 24% of precipitating. The rain in the green region, if any, is very light and may be contaminated by high liquid-content clouds. It is consistent with Lee et al. (2002) that the green region usually appears in the TC center with minimal rain and clouds.
5. RI events are led by an increase in all three hybrid pink (mainly stratiform rain) regions starting as early as 21–15 hr before RI (Figure 6d), followed by an increase of bright cyan (shallow convection; Figure 6a) starting around 3 hr before RI, and an increase of pure pink (deep convection; Figure 6b) starting around 3 hr after RI onset. This is consistent with previous studies showing that shallow-moderate convection (TJ15) and stratiform precipitation (Tao, 2015; Tao et al., 2017) could be a better indicator/predictor for subsequent RI than deep convection.

The results in this study not only confirm that the 37 GHz cyan + pink ring is mainly precipitative (KJ12; TJ15) but also provide a new way to separate different convective and stratiform precipitation types using satellite-based 37 GHz observations. Previously, the rain type classification mainly relies on radar observations, such as the TRMM 2A23 (Awaka et al., 2009). This new classification has the potential to be applied to passive microwave satellite observations, therefore improving the passive microwave rainfall retrieval algorithms.

Acknowledgments
The authors thank Margaret Kieper and Frank Marks and John Molinari for helpful insights and discussions on this work. The constructive comments from Dan Cecil and two anonymous reviewers are appreciated and contribute greatly in improving the manuscript. Support for this study was provided by NASA New Investigator Program (NIP) award NNX10AG55G, NASA Hurricane Science Research Program (HSRP) grant NNX10AG34G, and NASA Weather And Atmospheric Dynamics (WAAD) grant NNX17AH72G; NASA NESSF awards NNX11AP84H and NNX11AL66H under the direction of Ramesh Kakar and Ming-Ying Wei; and NOAA Joint Hurricane Testbed (JHT) grants NA11OAR4310193, NA13OAR4590191, NA15OAR4590199, and NA17OAR4590142 under the direction of Chris Landsea. The data used in this study are listed in the references, tables, and figures. Work at Lawrence Livermore National Laboratory (LLNL) was supported under the auspices of the U.S. Department of Energy by LLNL under contract DE-AC52-07NA27344.

References

Alvey, G. III, Zawislak, J., & Zipser, E. J. (2015). Precipitation properties observed during tropical cyclone intensity change. *Monthly Weather Review*, *143*(11), 4476–4492. https://doi.org/10.1175/MWR-D-15-0065.1

Awaka, J., Iguchi, T., & Okamoto, K. (2009). TRMM PR standard algorithm 2A23 and its performance on bright band detection. *Journal of the Meteorological Society of Japan*, *87A*, 31–52. https://doi.org/10.2151/jmsj.87A.31

Cecil, D. J., & Zipser, E. J. (2002). Reflectivity, ice scattering, and lightning characteristics of hurricane eyewalls and rainbands. Part II: Intercomparison of observations. *Monthly Weather Review*, *130*(4), 785–801. https://doi.org/10.1175/1520-0493(2002)130%3C0785:RISALC%3E2.0.CO;2

Cecil, D. J., Zipser, E. J., & Nesbitt, S. W. (2002). Reflectivity, ice scattering, and lightning characteristics of hurricane eyewalls and rainbands. Part I: Quantitative description. *Monthly Weather Review*, *130*(4), 769–784. https://doi.org/10.1175/1520-0493(2002)130%3C0769:RISALC%3E2.0.CO;2

Colwell, R. N. (1983). *Manual of remote sensing, volumes 1 and 2*. Falls Church, VA: American Society of Photogrammetry.

Dvorak (1975). Tropical cyclone intensity analysis and forecasting from satellite imagery. *Monthly Weather Review*, *103*(5), 420–430. https://doi.org/10.1175/1520-0493(1975)103%3C0420:TCIAAF%3E2.0.CO;2

Glickman, T. S. (Ed.) (2000). *Glossary of Meteorology* (2d ed., 855 pp.). American Meteorological Society.

Grody, N. C. (1993). In M. A. Janssen (Ed.), *Remote sensing of the atmosphere from satellites using microwave radiometry. Atmospheric Remote Sensing by Microwave Radiometry* (pp. 259–304). New York: John Wiley.

Hawkins, J. D., Lee, T. F., Turk, F. J., Sampson, C., Kent, J., & Richardson, K. (2001). Real-time Internet distribution of satellite products for tropical cyclone reconnaissance. *Bulletin of the American Meteorological Society*, *82*(4), 567–578. https://doi.org/10.1175/1520-0477(2001)082%3C0567:RIDOSP%3E2.3.CO;2

Hawkins, J. D., & Velden, C. (2011). Supporting meteorological field experiment missions and post-mission analysis with satellite digital data and products. *Bulletin of the American Meteorological Society*, *92*(8), 1009–1022. https://doi.org/10.1175/2011BAMS3138.1

Hence, D. A., & Houze, R. A. Jr. (2011). Vertical structure of hurricane eyewalls as seen by the TRMM Precipitation Radar. *Journal of the Atmospheric Sciences*, *68*(8), 1637–1652. https://doi.org/10.1175/2011JAS3578.1

Hence, D. A., & Houze, R. A. Jr. (2012). Vertical structure of tropical cyclone rainbands as seen by the TRMM Precipitation Radar. *Journal of the Atmospheric Sciences*, *69*(9), 2644–2661. https://doi.org/10.1175/JAS-D-11-0323.1

Hendricks, E. A., Montgomery, M. T., & Davis, C. A. (2004). The role of "vortical" hot towers in the formation of tropical cyclone Diana (1984). *Journal of the Atmospheric Sciences*, *61*(11), 1209–1232. https://doi.org/10.1175/1520-0469(2004)061%3C1209:TROVHT%3E2.0.CO;2

Hong, Y., Kummerow, C. D., & Olson, W. S. (1999). Separation of convective and stratiform precipitation using microwave brightness temperature. *Journal of Applied Meteorology*, *38*(8), 1195–1213.

Hoshino, S., & Nakazawa, T. (2007). Estimation of tropical cyclone's intensity using TRMM/TMI brightness temperature data. *Journal of the Meteorological Society of Japan*, *85*(4), 437–454. https://doi.org/10.2151/jmsj.85.437

Houze, R. A. Jr., Rasmussen, K. L., Zuluaga, M. D., & Brodzik, S. R. (2015). The variable nature of convection in the tropics and subtropics: A legacy of 16 years of the Tropical Rainfall Measuring Mission (TRMM) satellite. *Reviews of Geophysics*, *53*(3), 994–1021. https://doi.org/10.1002/2015RG000488

Iguchi, T., Kozu, T., Kwiatkwoski, J., Meneghini, R., Awaka, J., & Okamoto, K. (2009). Uncertainties in the rain profiling algorithm for the TRMM precipitation radar. *Journal of the Meteorological Society of Japan*, *87A*, 1–30. https://doi.org/10.2151/jmsj.87A.1

Jiang, H. (2012). The relationship between tropical cyclone intensity change and the strength of inner core convection. *Monthly Weather Review*, *140*(4), 1164–1176. https://doi.org/10.1175/MWR-D-11-00134.1

Jiang, H., Kieper M., & Pei Y. (2014), Improvement to the satellite-based 37 GHz ring rapid intensification index. 67th *Interdepartmental Hurricane Conference/Tropical Cyclone Research Forum*, Mar 4–7, 2014.

Jiang, H., Pei Y., Tao C., Kieper M., &, Zagrodnik J. (2015), Improvement to the satellite-based 37 GHz ring rapid intensification index—A year-2 update. 69th *Interdepartmental Hurricane Conference/Tropical Cyclone Research Forum*, Mar 2-5, 2015.

Jiang, H., Ramirez, E. M., & Cecil, D. J. (2013). Convective and rainfall properties of tropical cyclone inner cores and rainbands from 11 years of TRMM data. *Monthly Weather Review*, *141*(2), 431–450. https://doi.org/10.1175/MWR-D-11-00360.1

Johnson, R. H., Rickenbach, T. M., Rutledge, S. A., Ciesielski, P. E., & Schubert, W. H. (1999). Trimodal characteristics of tropical convection. *Journal of Climate*, *12*(8), 2397–2418.

Kaplan, J., & DeMaria, M. (2003). Large-scale characteristics of rapidly intensifying tropical cyclones in the North Atlantic basin. *Weather and Forecasting*, *18*(6), 1093–1108. https://doi.org/10.1175/1520-0434(2003)018%3C1093:LCORIT%3E2.0.CO;2

Kaplan, J., DeMaria, M., & Knaff, J. A. (2010). A revised tropical cyclone rapid intensification index for the Atlantic and eastern North Pacific basins. *Weather and Forecasting*, *25*(1), 220–241. https://doi.org/10.1175/2009WAF2222280.1

Kida, S., Shige, S., Kubota, T., Aonashi, K., & Okamoto, K. I. (2009). Improvement of rain/no-rain classification methods for microwave radiometer observations over the ocean using a 37 GHz emission signature. *Journal of the Meteorological Society of Japan. Ser. II*, *87*, 165–181.

Kieper, M., & Jiang, H. (2012). Predicting tropical cyclone rapid intensification using the 37 GHz ring pattern identified from passive microwave measurements. *Geophysical Research Letters*, *39*, L13804. https://doi.org/10.1029/2012GL052115

Lee, T. F., Turk, F. J., Hawkins, J., & Richardson, K. (2002). Interpretation of TRMM TMI images of tropical cyclones. *Earth Interactions*, *6*(3), 1–17. https://doi.org/10.1175/1087-3562(2002)006%3C0001:IOTTIO%3E2.0.CO;2

Liu, C., Zipser, E. J., Cecil, D. J., Nesbitt, S. W., & Sherwood, S. (2008). A cloud and precipitation feature database from 9 years of TRMM observations. *Journal of Applied Meteorology and Climatology*, *47*(10), 2712–2728. https://doi.org/10.1175/2008JAMC1890.1

Molinari, J., & Vollaro, D. (2010). Rapid intensification of a sheared tropical storm. *Monthly Weather Review*, *138*(10), 3869–3885. https://doi.org/10.1175/2010MWR3378.1

Montgomery, M. T., Nicholls, M. E., Cram, T. A., & Saunders, A. B. (2006). A vortical hot tower route to tropical cyclogenesis. *Journal of the Atmospheric Sciences*, *63*(1), 355–386. https://doi.org/10.1175/JAS3604.1

Negri, A. I., Adler, R. F., & Kummerow, C. D. (1989). False-color display of Special Sensor Microwave/Imager (SSM/I). *Bulletin of the American Meteorological Society*, *70*(2), 146–151. https://doi.org/10.1175/1520-0477(1989)070%3C0146:FCDOSS%3E2.0.CO;2

Nolan, D. S., & Grasso, L. D. (2003). Nonhydrostatic, three- dimensional perturbations to balanced, hurricane-like vortices. Part II: Symmetric response and nonlinear simulations. *Journal of the Atmospheric Sciences*, *60*(22), 2717–2745. https://doi.org/10.1175/1520-0469(2003)060%3C2717:NTPTBH%3E2.0.CO;2

Petersen, R. A., Uccellini, L. W., Mostek, A., & Keyser, D. A. (1984). Delineating mid- and low-level water vapor patterns in pre-convective environments. *Monthly Weather Review*, *112*(11), 2178–2198. https://doi.org/10.1175/1520-0493(1984)112%3C2178:DMALLW%3E2.0.CO;2

Rappaport, E. N., & Coauthors (2009). Advances and challenges at the National Hurricane Center. *Weather and Forecasting*, *24*(2), 395–419. https://doi.org/10.1175/2008WAF2222128.1

Reasor, P. D., Eastin, M. D., & Gamache, J. F. (2009). Rapidly intensifying Hurricane Guillermo (1997). Part I. Low-wavenumber structure and evolution. *Monthly Weather Review*, *137*(2), 603–631. https://doi.org/10.1175/2008MWR2487.1

Rogers, R. F., Reasor, P. D., & Lorsolo, S. (2013). Airborne Doppler observations of the inner-core structural differences between intensifying and steady-state tropical cyclones. *Monthly Weather Review*, *141*(9), 2970–2991. https://doi.org/10.1175/MWR-D-12-00357.1

Rogers, R. F., Reasor, P. D., & Zhang, J. A. (2015). Multiscale structure and evolution of hurricane earl (2010) during rapid intensification. *Monthly Weather Review*, *143*(2), 536–562. https://doi.org/10.1175/MWR-D-14-00175.1

Schumacher, C., & Houze, R. A. Jr. (2003). The TRMM Precipitation Radar's view of shallow, isolated rain. *Journal of Applied Meteorology*, *42*(10), 1519–1524. https://doi.org/10.1175/1520-0450(2003)042%3C1519:TTPRVO%3E2.0.CO;2

Short, N. M., Lowman, P. D. Jr., Freden, S. C., & Finch, W. A. (1976). *Mission to Earth: Landsat views the world* (NASA Technical Report SP-360). Washington, DC: National Aeronautics and Space Administration.

Spencer, R. W. (1986). A satellite passive 37-GHz scattering-based method for measuring oceanic rain rates. *Journal of Climate and Applied Meteorology*, *25*(6), 754–766. https://doi.org/10.1175/1520-0450(1986)025%3C0754:ASPGSB%3E2.0.CO;2

Spencer, R. W., Goodman, H. M., & Hood, R. E. (1989). Precipitation retrieval over land and ocean with the SSM/I: Identification and characteristics of the scattering signal. *Journal of Atmospheric and Oceanic Technology*, *6*(2), 254–273. https://doi.org/10.1175/1520-0426(1989)006%3C0254:PROLAO%3E2.0.CO;2

Steiner, M., Houze, Jr. R. A., & Yuter, S. E. (1995). Climatological characterization of three-dimensional storm structure from operational radar and rain gauge data. *Journal of Applied Meteorology*, *34*(9), 1978–2007.

Stevenson, S. N., Corbosiero, K. L., & Molinari, J. (2014). The convective evolution and rapid intensification of Hurricane Earl (2010). *Monthly Weather Review*, *142*(11), 4364–4380. https://doi.org/10.1175/MWR-D-14-00078.1

Susca-Lopata, G., Zawislak, J., Zipser, E. J., & Rogers, R. F. (2015). The role of observed environmental conditions and precipitation evolution in the rapid intensification of Hurricane Earl (2010). *Monthly Weather Review*, *143*(6), 2207–2223. https://doi.org/10.1175/MWR-D-14-00283.1

Tao, C. (2015). Climatology of overshootings in tropical cyclones and their roles in tropical cyclone intensity change using TRMM data (PhD dissertation) (193 pp.). Florida International University.

Tao, C., & Jiang, H. (2013). Global distribution of hot towers in tropical cyclones based on 11-year TRMM data. *Journal of Climate*, *26*(4), 1371–1386. https://doi.org/10.1175/JCLI-D-12-00291.1

Tao, C., & Jiang, H. (2015). Distributions of shallow to very deep convection in rapidly intensifying tropical cyclones. *Journal of Climate*, *28*(22), 8791–8824. https://doi.org/10.1175/JCLI-D-14-00448.1

Tao, C., Jiang, H., & Zawislak, J. (2017). The relative importance of Stratiform and convective rainfall in rapidly intensifying tropical cyclones. *Monthly Weather Review*, *145*(3), 795–809. https://doi.org/10.1175/MWR-D-16-0316.1

Weng, F., & Grody, N. C. (1994). Retrieval of cloud liquid water using the special sensor microwave imager (SSM/I). *Journal of Geophysical Research*, *99*(D12), 25,535–25,551. https://doi.org/10.1029/94JD02304

Wu, R., & Weinman, J. A. (1984). Microwave radiances from precipitating clouds containing aspherical ice, combined phase, and liquid hydrometeors. *Journal of Geophysical Research*, *89*(D5), 7170–7178. https://doi.org/10.1029/JD089iD05p07170

Yuter, S. E., & Houze, R. A. (1995). Three-dimensional kinematic and microphysical evolution of Florida cumulonimbus. Part II: Frequency distributions of vertical velocity, reflectivity, and differential reflectivity. *Monthly Weather Review*, *123*(7), 1941–1963. https://doi.org/10.1175/1520-0493(1995)123%3C1941:TDKAME%3E2.0.CO;2

Zagrodnik, J., & Jiang, H. (2014). Rainfall, convection, and latent heating distributions in rapidly intensifying tropical cyclones. *Journal of the Atmospheric Sciences*, *71*(8), 2789–2809. https://doi.org/10.1175/JAS-D-13-0314.1

Zawislak, J., & Zipser, E. J. (2014). A multisatellite investigation of the convective properties of developing and nondeveloping tropical disturbances. *Monthly Weather Review*, *142*(12), 4624–4645. https://doi.org/10.1175/MWR-D-14-00028.1

Zawislak, J., Jiang, H., Alvey III, G. R., Zipser, E. J., Rogers, R. F., Zhang, J. A., & Stevenson, S. N. (2016). Observations of the structure and evolution of Hurricane Edouard (2014) during intensity change. Part I: Relationship between the thermodynamic structure and precipitation. *Monthly Weather Review*, *144*(9), 3333–3354.

Zipser, E. J., Cecil, D., Liu, C., Nesbitt, S., & Yorty, D. (2006). Where are the most intense thunder storms on Earth? *Bulletin of the American Meteorological Society*, *87*(8), 1057–1072. https://doi.org/10.1175/BAMS-87-8-1057